

Ultrathin Second-Harmonic Metasurfaces with Record-High Nonlinear Optical Response

Jongwon Lee, Nishant Nookala, J. Sebastian Gomez-Diaz, Mykhailo Tymchenko, Frederic Demmerle, Gerhard Boehm, Markus-Christian Amann, Andrea Alù, and Mikhail A. Belkin*

Ultrathin (subwavelength thickness) nonlinear metasurfaces have recently been put forward to achieve super-resolution imaging,^[1] implement nonlinear photonic crystal structures,^[2] enable optical switching and memories at the nanoscale,^[3] produce frequency mixing with relaxed phase-matching constraints,^[4] and allow control of the output wavefront by continuously tailoring the phase of the local nonlinear response.^[5–10] However, the level of nonlinear responses enabled by traditional materials, such as metals and dielectric crystals,^[11,12] and metasurfaces based on metallic nanoresonator^[2,6,13,14] is far too weak to enable in practice a flat nonlinear optics paradigm,^[4,5] based on which properly designed ultrathin metasurfaces provide efficient frequency conversion without the conventional phase-matching constraints of bulk nonlinear crystals,^[4] and have the ability to manipulate the wavefront of the nonlinear signal output with subwavelength resolution, enabling advanced functionalities such as beam-steering or focusing.^[2,5–10] Here, we experimentally demonstrate nonlinear metasurfaces for mid-infrared second-harmonic generation (SHG) with the second-order nonlinear susceptibility of 1.2×10^6 pm V⁻¹, to the best of our knowledge the largest value of second-order nonlinear response in infrared/visible spectral range reported for a condensed matter system and 3–5 orders of magnitude higher than that of traditional nonlinear materials and nonlinear metasurfaces based on plasmonic nanoresonators. Giant nonlinear response of our structures enables efficient frequency mixing in optical films of subwavelength thickness using pump intensity well below materials damage threshold.

It can be shown (see the Supporting Information) that the power conversion efficiency η for SHG in a phase-matched nonlinear medium of thickness d is given by

$$\eta \equiv \frac{I_{2\omega}}{I_{\omega}} = \frac{\pi^2}{n_{\omega} n_{2\omega}} \left(\frac{d}{\lambda_{2\omega}} \right)^2 |\chi_{\text{eff}}^{(2)} E_{\omega}|^2 \approx \left(\frac{d}{\lambda_{2\omega}} \right)^2 |\chi_{\text{eff}}^{(2)} E_{\omega}|^2, \quad (1)$$

where ω , n_{ω} , I_{ω} (2ω , $n_{2\omega}$, $I_{2\omega}$) are the fundamental (second-harmonic) frequency, refractive index, and intensity, respectively, $\chi_{\text{eff}}^{(2)}$ is the effective nonlinear susceptibility for a particular input–output polarization combination, E_{ω} is the pump electric field, $\lambda_{2\omega}$ is the second harmonic (SH) wavelength, and we have used the undepleted pump approximation.^[11,12] Equation (1) shows that, in order to provide high nonlinear conversion efficiency in films of subwavelength thickness, we need to have $|\chi_{\text{eff}}^{(2)} E_{\omega}| \approx 1$ or, in other words, the nonlinear polarization $\bar{P}^{(2)} = \epsilon_0 \bar{\chi}^{(2)} \bar{E}_{\omega} \bar{E}_{\omega}$ must become comparable to the linear one $\bar{P} = \epsilon_0 \bar{\chi}^{(1)} \bar{E}_{\omega}$, where $\bar{\chi}^{(1)} \approx 1$ is the linear susceptibility. Similar conclusions may be drawn for other three-wave mixing processes (sum- or difference-frequency generation), and for higher-order nonlinear processes.

Traditional nonlinear materials^[11,12] and nonlinear metasurfaces based on plasmonic nanoresonators previously demonstrated in the infrared/visible frequencies^[2,6,13,14] have second-order nonlinear elements in the range 1–1000 pm V⁻¹. Pump intensities ranging from 0.1 TW cm⁻² to over 100 PW cm⁻² and optical fields comparable to atomic fields^[11,12] are needed to achieve condition $|\chi_{\text{eff}}^{(2)} E_{\omega}| \approx 1$. Such intensities are only possible with high-power ultrafast lasers, and are typically well above the materials damage threshold. In particular, SHG power conversion efficiencies below 10⁻¹⁰ were reported for ultrathin nonlinear metasurfaces pumped with femtosecond pulses with intensities as high as 0.1 GW cm⁻² in refs. [2,6,13,14].

We have recently reported a different approach to realize nonlinear metasurfaces based on coupling of electromagnetic modes in metallic nanoresonators with quantum-engineered intersubband nonlinearities in multi-quantum-well (MQW) semiconductor heterostructures.^[4] This approach allows one to convert giant nonlinear susceptibility of MQW heterostructures ($\chi_{\text{MQW},zzz}^{(2)}$), which is intrinsically polarized in the z -direction normal to the surface,^[15–23] into any in-plane element $\chi_{ijk}^{(2)}$ ($i, j = x$ or y) of the nonlinear susceptibility tensor of the metasurface. The metallic nanoresonators resonantly couple to the impinging pump field at the fundamental frequency and produce a strong component of the electric field normal to the surface at the fundamental frequency in the MQW layer. This electric field produces second-order nonlinear polarization at the SH frequency in the MQW layer. The oscillating nonlinear polarization couples to the nanoresonators resonant mode at SH frequency, and the SH radiation is efficiently out-coupled to the free space by the nanoresonators.^[4] We note that

Prof. J. Lee,^[†] N. Nookala, Dr. J. S. Gomez-Diaz, M. Tymchenko, Prof. A. Alù, Prof. M. A. Belkin
Department of Electrical and Computer Engineering
University of Texas at Austin
Austin, TX 78712, USA
E-mail: mbelkin@ece.utexas.edu

F. Demmerle, G. Boehm, Prof. M.-C. Amann
Walter Schottky Institut
Technische Universität München
Am Coulombwall 4, Garching 85748, Germany

^[†]Present address: School of Electrical and Computer Engineering, Ulsan National Institute of Science and Technology (UNIST), Ulsan 44919, South Korea

DOI: 10.1002/adom.201500723



nonlinear metasurfaces operating in transmission and based on nanoresonators with different geometries have also been reported recently.^[7] We have speculated^[4] that the nanoresonators may be used to produce in-plane elements of the metasurface nonlinear susceptibility tensor that exceed the values of intrinsic MQW nonlinearity $\chi_{MQW,zzz}^{(2)}$. However, this was very hard to achieve in practice with metal nanoresonators and the largest nonlinear coefficient of the metasurface measured experimentally in ref. [4] was only $5 \times 10^4 \text{ pm V}^{-1}$, below the intrinsic nonlinearity of the MQW structure employed in that work.

In this work, we experimentally demonstrate a MQW-based nonlinear metasurface that utilize metal-semiconductor nanocavities. Unlike metal nanoresonators used previously, metal-semiconductor nanocavities not only convert z -polarized MQW nonlinear susceptibility into transverse plane but provide further enhancement to the nonlinear response. Combined with innovations in the MQW design, this approach allowed us to produce a metasurface with record value of second-order nonlinear optical response of $1.2 \times 10^6 \text{ pm V}^{-1}$, more than 20 times that reported in ref. [4]. Such metasurfaces fulfill the condition $|\chi_{\text{eff}}^{(2)} E_{\omega}| \approx 1$ for pump intensities well below 1 MW cm^{-2} and can realistically provide over 2.5% SHG power conversion efficiency for only a few tens of kW cm^{-2} of optical pumping intensity and $\lambda/25$ nonlinear layer thickness. Experimentally, we demonstrate 0.075% SHG power conversion efficiency with 400-nm-thick metasurfaces pumped with $\lambda \approx 10 \mu\text{m}$ radiation with 15 kW cm^{-2} pump intensity.

Figure 1a shows the band diagram of a coupled quantum well structure, repeated multiple times to produce a 400-nm-thick MQW layer used in our work. The thickness d of the MQW layer in our case is chosen so as to maximize the product of $|\chi_{\text{eff}}^{(2)}| \cdot d$ in Equation (1) (see the discussion below for details of computing of $\chi_{\text{eff}}^{(2)}$). The values of energies ($\hbar\omega_{ij}$) and transition dipole moments (ez_{ij}) for transitions between the first three electron subbands ($i, j = 1, 2, 3$) are shown in figure. The structure is designed to support giant resonant nonlinear SHG at the optimal pump wavenumber $1/\lambda \approx 1000 \text{ cm}^{-1}$ ($\lambda \approx 10 \mu\text{m}$ or 124 meV photon energy). Figure 1b plots the absolute value of the nonlinear susceptibility tensor element $\chi_{MQW,zzz}^{(2)}$ as a function of pump wavenumber or wavelength calculated for a bare

MQW structure assuming low pump intensity as described in the Experimental Section. The nonlinear response peaks at approximately $2.8 \times 10^5 \text{ pm V}^{-1}$, 3–4 orders of magnitude larger than the largest $\chi^{(2)}$ coefficient of natural optical materials.^[11,12]

Unlike doubly resonant MQW designs ($\hbar\omega_{21} = \hbar\omega_{32} = \hbar\omega_{31}/2$) used in MQW-based metasurfaces previously,^[4,7] the transition energy between states 1 and 2 in the MQW design used in this work is purposely detuned by approximately 25 meV from the optimal pump photon energy of $\hbar\omega \approx 124 \text{ meV}$ to reduce optical losses in the nanoresonator cavity and avoid saturation of nonlinear optical response by pump light. Saturation in MQWs occurs when the input intensity is so large that the intersubband absorption empties the quantum well ground state, reducing the nonlinear response of the MQW system.^[22,24–26] Theoretical analysis presented by us in refs. [4,24] indicated that saturation of MQW nonlinearity by pump intensity imposes fundamental limits to the conversion efficiency in MQW-based nonlinear metasurfaces and MQW structures with 1–2 transition detuned from the pump frequency and 1–3 transition coinciding with the second harmonic frequency provide optimal performance.

The MQW layer is transferred onto a metal ground plane by wafer bonding/substrate removal procedure. A pattern of metal-semiconductor nanocavities is then defined in the MQW layer as shown in Figure 1c. Details of the processing are given in the Experimental Section. The nanocavity configuration enables efficient coupling of x -polarized impinging field beam at fundamental frequency and y -polarized outgoing wave at SH frequency to z -polarized MQW intersubband transitions as discussed in the following.

Figure 2a shows the normalized E_z field component induced in the MQW layer for x -polarized fundamental and y -polarized SH light at normal incidence, which represents the optimal SHG polarization combination for our metasurface design. The computed fields are normalized to the input (transverse) field amplitude, and simulations show up to 16 times local field enhancement in the MQW layer. Figure 2b confirms that the proposed antenna structure possesses strong resonances at both frequencies of interest. The overall nonlinear response of the proposed metasurface can be obtained by computing its nonlinear susceptibility tensor $\chi_{ijk}^{(2)}$ using the expression^[4]

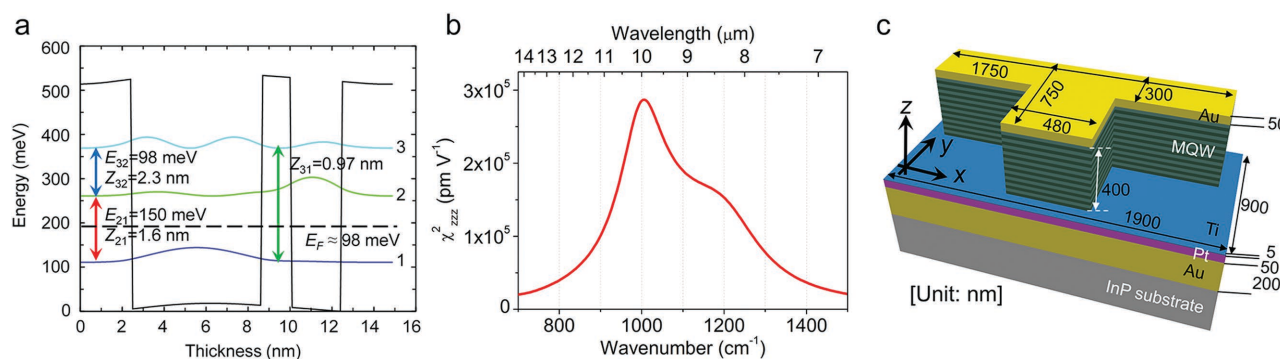


Figure 1. Nonlinear metasurface structure. a) Conduction band diagram of one period of an $\text{In}_{0.53}\text{Ga}_{0.47}\text{As}/\text{Al}_{0.48}\text{In}_{0.52}\text{As}$ coupled quantum well structure designed for giant nonlinear response for SHG. b) Intersubband nonlinear susceptibility of the structure in panel (a) as a function of pump frequency for SHG. c) A $1.9 \mu\text{m}$ by $0.9 \mu\text{m}$ metasurface unit-cell.

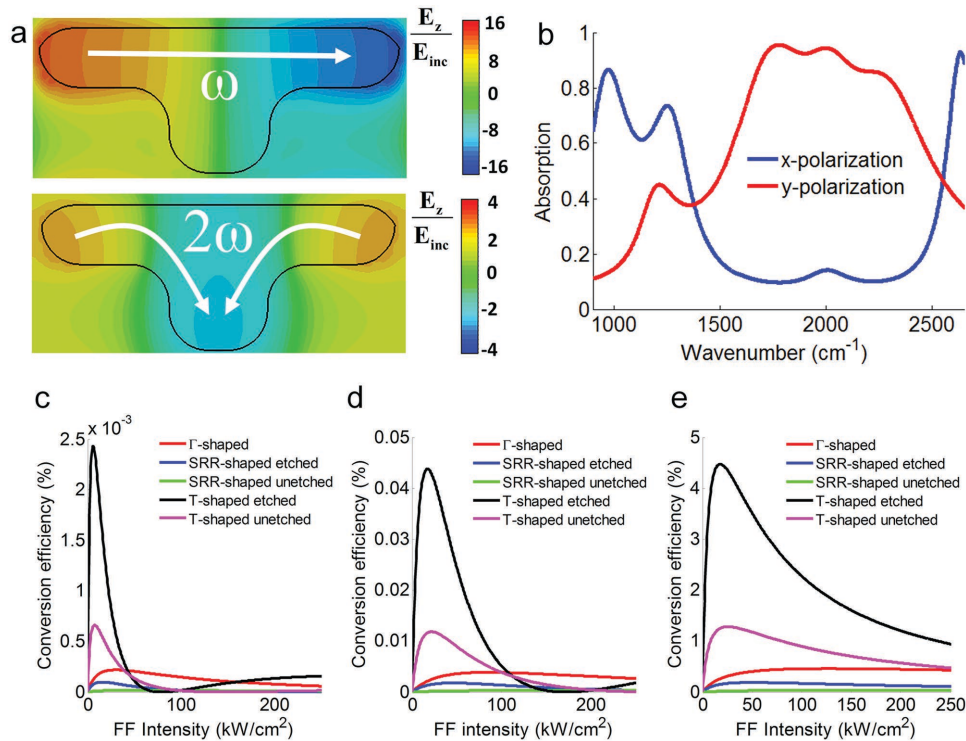


Figure 2. Numerical simulations of plasmonic nonlinear metasurfaces. a) Top view of the normalized E_z field distribution on the T-shaped resonator at the pump and second harmonic frequencies. b) Absorption spectrum of the proposed metasurface for different polarization of the incident light. c–e) Metasurface conversion efficiency for several types of resonators and MQW configurations versus pump intensity. The geometries considered are the Γ -shaped structure described in ref. [4], the T-shaped resonator proposed here, with and without etching, the etched SRR operating in reflection described in ref. [5] and the unetched SRR operating in transmission of ref. [7]. The multi-quantum-well configurations are described in ref. [4] for panel (c) and in Figure 1 for panel (d). Panel (e) considers a similar MQW structure as panel (d) but assumes intersubband transition linewidths of 10 meV FWHM for all transitions.

$$\chi_{ijk}^{(2)} = \chi_{\text{MQW},zzz}^{(2)} \left[\frac{\int_{\text{UC}} \xi_i^{2\omega}(x,y,z) \xi_j^\omega(x,y,z) \xi_k^\omega(x,y,z) dV}{V} \right], \quad (2)$$

where ξ_i^ω ($\xi_i^{2\omega}$) is the local enhancement of the induced z-polarized E-field in the MQW structure normalized to the i -polarized incident wave ω (2ω), and the expression in square brackets is the nonlinear overlap integral between fundamental and second harmonic modes of the nanoantenna^[4] with the integration going over the entire unit-cell volume. Equation (2) shows that maximizing value of the overlap integral is the key parameter in the nonlinear metasurface design.

In contrast to the resonators used previously,^[4,7] which were made by metal patterning on top of a continuous MQW layer, the resonators used in this work are open metal-semiconductor nanocavities as shown in Figure 1c. This solution significantly contributes to enhance the modal overlap integral, due to the large contrast between the permittivity of the MQW substrate and the air gaps, by i) improving the uniformity of the induced field distribution in the MQW regions at both fundamental and second harmonic frequencies, ii) concentrating most of the electric field within the nanocavity, and iii) enhancing the maximum local electric field. We chose nanocavities with a T-shaped geometry that allows the independent control of the fundamental (long arm along the x -axis) and second harmonic (dipole created between the short and long arm) resonances,

as illustrated in Figure 2a. In addition, we have minimized the unit cell footprint, rigorously taken into account cross-coupling effects between adjacent nanoresonators. The adequate combination of all these factors allows a modal overlap integral above 4.25, around eight times larger than the one obtained in ref. [4] and nearly 30 times larger than that obtained for the structures reported in ref. [7]. Interestingly, this enhancement is realized by removing nonlinear material from the structure, to force the modal fields to be more localized within the volume directly underneath the resonator, maximizing the overlap at the two frequencies.

In order to further highlight the significant improvements on the MQW and nanoresonator designs achieved here, in Figure 2c–e, we show the theoretically predicted SHG conversion efficiency as a function of pump intensity. Our simulations fully incorporate local saturation of intersubband nonlinearity following the approach described in ref. [24]. We investigate the Γ -shaped nanostructures presented in ref. [4] and the splitting resonators (SRR) described in ref. [7] and in ref. [5] and we compare them to the T-shaped geometry proposed here. In order to illustrate how etching the nanoresonator enhances the response of nonlinear metasurfaces, we consider SRR and T-shaped geometries with and without etching the MQW layer. The results are computed considering different multi-quantum-well configurations: The semiconductor heterostructure described in ref. [4] (Figure 2c), the MQW detailed above

(Figure 2d) with experimentally measured transition linewidths of approximately 25–30 meV full-width-half-maximum (FWHM) as described in the Supporting Information and with $\chi_{\text{MQW},zzz}^{(2)}$ values shown in Figure 1b, and similar MQW structures (see Figure 2e) with linewidth reduced to 10 meV FWHM. We note that transition linewidths of 10 meV FWHM were reported previously in heavily doped semiconductor heterostructures at room temperature, and even narrower linewidths were reported from heavily doped MQW structures at cryogenic temperatures.^[27,28] Our numerical simulations show that, with the current nanoresonator and MQW designs, the conversion efficiency can reach values above 2.5%, assuming that transition linewidths of 10 meV FWHM can be achieved in our MQW structures. Further improvements are expected with more advanced nanoresonator and MQW designs.

Experimentally, we fabricate a 400 μm by 400 μm metasurface using the unit cell design shown in Figure 1c (fabrication details are provided in the Experimental Section). Figure 3a shows the scanning electron microscope image of the processed structure. The nonlinear response was tested using the experimental setup shown in Figure 3b and described in figure

caption. The linear reflection absorption spectra measured for normally incident x - and y -polarized light are shown in the inset of Figure 3c. Strong absorption at fundamental and SH frequency is observed for x - and y -polarized inputs, respectively, in good agreement with theory. Figure 3c shows SHG peak power as a function of the squared fundamental peak power and peak intensity for γ_{xx} polarization combination, where the first letter refers to the polarization of the generated SH beam and the other two refer to the polarization states of the pump beams. Other polarization combinations provide much smaller SHG response, since our nanoresonators only provide coupling of incident/outgoing waves to the MQW for x -polarized light at fundamental frequency and y -polarized light at SH frequency (see inset of Figure 3c). From Equation (1) one expects to observe a linear dependence of SH power on the square of the pump power in Figure 3c. However, the slope of the curve in Figure 3c changes from 16.8 mW W^{-2} for low input powers to 5.3 mW W^{-2} for higher pump power due to intensity saturation.^[4,24]

The experimentally measured SHG power conversion efficiency, defined in Equation (1), as a function of pump intensity,

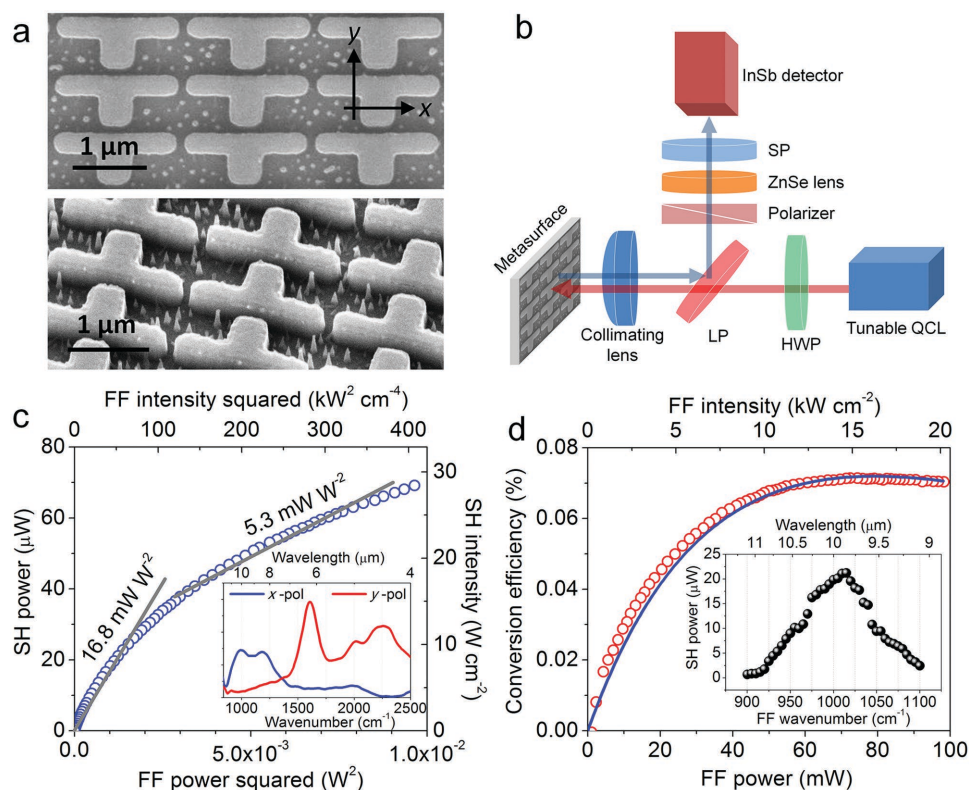


Figure 3. Experimental measurements of the nonlinear response from a metasurface. a) Scanning electron microscope images of the fabricated metasurface. Top panel represents the top view and the bottom panel is a view at 30° from the surface normal. b) Optical setup for metasurface characterization. Linearly polarized light beam from a wavelength-tunable quantum cascade laser (QCL) passes through achromatic half-wave plate for polarization control, a long-pass dichroic beamsplitter (LP) to remove SHG light coming from the laser, transmit input pump to the sample, and reflect SHG light from the metasurface to the detector, a numerical aperture 0.5 collimating lens to the sample. SHG output is collected by the same lens and is directed by the LP toward the detector through a polarizer, a ZnSe lens, and a short pass filter that is used to block the pump frequency. c) SH peak power (left axis) or peak intensity (right axis) as a function of fundamental peak power squared (bottom axis) or peak intensity squared (top axis) at pump wavenumber of 1015 cm^{-1} ($\lambda\omega \approx 9.9 \mu\text{m}$) for γ_{xx} polarization combination. Inset: reflection-absorption spectra of metasurface for x - and y -polarized light. d) Experimentally measured (red circles) and theoretically calculated (blue solid line) SHG power conversion efficiency as a function of fundamental peak power (bottom axis) or peak intensity (top axis) at wavenumber of 1015 cm^{-1} for γ_{xx} polarization combination. Inset: SH peak power as a function of pump wavenumber for γ_{xx} polarization combination. Pump peak power was fixed at 35 mW for the measurements.

is shown in Figure 3d together with our theoretical predictions, assuming $\chi_{\text{MQW},zzz}^{(2)} \approx 3.5 \times 10^5 \text{ pm V}^{-1}$, 25% higher than that computed theoretically in Figure 1b. We note that this discrepancy could be due to the actual values of transition dipole moments slightly different from that computed theoretically or because of the transition linewidth for 2 to 3 transition is different from that assumed (see the Experimental Section for details of theoretical calculations of $\chi_{\text{MQW},zzz}^{(2)}$). Excellent agreement between experiment and theory is observed. In our numerical simulations, we have kept the theoretical modal overlapping integral and electromagnetic response of the plasmonic nanocavities (see Figure 2 and the Supporting Information), and only modified the intrinsic MQW nonlinearity to fit the experiments. This allows to indirectly deduce an intrinsic MQW intersubband susceptibility of $\chi_{\text{MQW},zzz}^{(2)} \approx 3.5 \times 10^5 \text{ pm V}^{-1}$ for low pump intensities, which is in good agreement with the theoretical results of Figure 1b, given the uncertainties in theoretical computations and measurement processes.

The value of $\chi_{\text{yxz}}^{(2)}$ can be obtained using the data in Figure 3c and Equation (1) as described in the Supporting Information. We obtain $\chi_{\text{yxz}}^{(2)} \approx 1.2 \times 10^6 \text{ pm V}^{-1}$ ($0.7 \times 10^6 \text{ pm V}^{-1}$) for low (high) pump intensity in Figure 3c. These numbers represent the largest values of second-order nonlinear susceptibility ever recorded to our knowledge in the IR–vis range in a condensed matter system. In comparison, the nonlinear response of the best traditional nonlinear materials in IR–vis range is in the range $1\text{--}1000 \text{ pm V}^{-1}$.^[11,12] Such giant values of optical nonlinearity allows us to achieve 0.075% conversion efficiency from 400-nm-thick MQW layer using pump intensity in the range $10\text{--}15 \text{ kW cm}^{-2}$, as shown in Figure 3d.^[29]

The values of conversion efficiencies achieved in our structures are already sufficient for practical applications, such as optical gating or second-order autocorrelation characterization of mid-infrared pulses. In particular, our metasurfaces may be used for pulse characterization of mid-infrared quantum cascade lasers, instead of cryogenically cooled two-photon photodetectors.^[30] Due to subwavelength thickness, phase matching in the direction normal to the surface of our metasurfaces is no longer important and phase matching is always automatically satisfied for wave vector components parallel to the slab for any input frequencies and incidence angles. This relaxation of the phase matching requirements significantly simplifies the realization of many nonlinear optical experiments. Improvements in metasurface design and MQW material quality is expected to lead to even higher conversion efficiencies as discussed in Figure 2. This will facilitate the practical development of a flat nonlinear paradigm, with exciting applications such as beam steering, focusing, or the generation of nonlinear vortex beams.^[2,5–10]

We note that the metasurfaces reported here can be tailored for operation anywhere in the entire mid- and far-infrared spectral range ($\lambda = 3\text{--}30 \text{ }\mu\text{m}$ and $30\text{--}300 \text{ }\mu\text{m}$, respectively). They may be used for a wide range of applications, such as to perform optical gating (e.g., for spectroscopic applications and light detection and ranging), to extend the spectral range of mid-infrared and THz laser sources (e.g., by frequency doubling or via sum-frequency or difference-frequency generation), to provide nonlinear medium for autocorrelation short-pulse characterization, as well as up-conversion (via sum-frequency

generation) from one spectral range to the other for detection and imaging.

In summary, we have demonstrated metasurfaces based on metal-MQW semiconductor nanocavities with the second-order nonlinear susceptibility of $1.2 \times 10^6 \text{ pm V}^{-1}$. Our work demonstrates the feasibility of achieving efficient frequency mixing in optical films of subwavelength thickness using pumping intensity well below materials damage threshold even for continuous-wave excitation. These results open a new paradigm in nonlinear optics, based on which efficient frequency conversion may be achieved in deeply subwavelength metasurfaces with greatly relaxed phase-matching conditions and with the possibility of controlling the output wavefront at the individual nanoresonator level with deeply subwavelength resolution.^[5]

Experimental Section

Device Growth and Fabrication: The $\text{In}_{0.53}\text{Ga}_{0.47}\text{As}/\text{Al}_{0.48}\text{In}_{0.52}\text{As}$ coupled quantum well structure for nonlinear response shown in Figure 1b was designed using a self-consistent Poisson–Schrodinger solver. The layer sequence (in nanometer) is **2.5/6.2/1.4/2.4/2.5** where AlInAs barriers are shown in bold, and the first 1.5 nm of the first 2.5-nm-barrier and the last 1.5 nm of the last 2.5-nm-barrier are n-doped to $6 \times 10^{18} \text{ cm}^{-3}$. A 390-nm-thick MQW layer composed of 26 repetitions of the structure in Figure 1a was grown by the molecular beam epitaxy on a semi-insulating InP substrate. The growth started with a 300-nm-thick etch-stop layer of $\text{In}_{0.53}\text{Ga}_{0.47}\text{As}$, followed by a 100-nm-thick etch-stop layer of InP, and followed by the MQW layer. A 10-nm-thick layer of titanium, a 50-nm-thick layer of platinum, and a 200-nm-thick layer of gold were sequentially evaporated on top of the MQW layer. The wafer was then thermocompressively bonded epi-side down to a semi-insulating InP wafer coated with same metal layers. The substrate was removed via selective chemical wet-etching, followed by the removal of the etch-stop layers via selective wet-etching to expose the MQW layer. A 5-nm-thick layer of titanium and 50-nm-thick layer of gold were evaporated on the top exposed MQW layer, followed by plasma enhanced chemical vapor deposition of a 250-nm-thick silicon nitride (SiN) hard-mask layer. Nanoresonators were then patterned on the silicon nitride layer via electron beam lithography and the patterns were etched through the silicon nitride layer and the MQW layer via inductively coupled plasma reactive ion plasma etching, followed by selective removal of the silicon nitride mask layer.

We note that because electron dynamics of intersubband transitions is determined by extremely fast ($\approx 0.3\text{--}3 \text{ ps}$) longitudinal optical photon scattering, surface defects introduced virtually no change in electron scattering times. As a result, unlike interband (electron–hole) transitions, intersubband transitions are virtually unaffected by surface defects as one etches through the MQW heterostructure. This property has allowed fabrication of a variety of deep-etched multiquantum-well devices without sacrificing device performance, see, e.g., refs. [31,32].

Quantum confinement due to etching is also not expected to influence intersubband transition energies, unless the transverse dimensions of the etched structures are comparable to the quantum well size ($\approx 2\text{--}3 \text{ nm}$). The smallest feature size of our nanoresonator is $\approx 300 \text{ nm}$, and such dimension introduces smaller than 1 meV shift of electron subband energies due to quantum confinement. Thus, from the perspective of quantum confinement, the nanoresonator width fluctuation is expected to produce intersubband transition energy fluctuation of much less than 1 meV.

Optical Measurements: Linear optical characterization of the metasurface was done in reflection mode using a Fourier-transform infrared spectrometer equipped with a liquid nitrogen cooled Mercury Cadmium Telluride photodetector. Nonlinear optical characterization of the metasurface was probed by a pulsed broadly wavelength-tunable quantum cascade laser (Daylight Solutions, Inc.; tuning range $900\text{--}1190 \text{ cm}^{-1}$ and

the peak power output of 350 mW). The pump focal spot diameter on the metasurface was measured by the knife-edge technique to be $2\omega = 35 \mu\text{m}$. The laser was operated with 400 ns long pulses at 250 kHz repetition frequency. A calibrated InSb detector was used to measure SHG power output and perform spectroscopic measurements at SHG frequencies. Calibrated thermopile detector was used to determine the power of the fundamental beam at the sample position.

MQW Nonlinearity Calculation: The value of $\chi_{\text{MQW},\text{zzz}}^{(2)}$ shown in Figure 1b was computed considering only the first three electron subbands as shown in Figure 1a using the equation^[11,12,15]

$$\chi_{\text{MQW},\text{zzz}}^{(2)}(\omega \rightarrow 2\omega) = N_e \frac{e^3}{\epsilon_0 \hbar} \left\{ \frac{z_{12}z_{23}z_{31}}{(\omega_{21} - 2\omega - i\gamma_{21})(\omega_{31} - \omega - i\gamma_{31})} + \frac{z_{12}z_{23}z_{31}}{(\omega_{32} - 2\omega - i\gamma_{32})(\omega_{21} + \omega + i\gamma_{21})} + \frac{z_{12}z_{23}z_{31}}{(\omega_{23} + 2\omega + i\gamma_{23})(\omega_{31} - \omega - i\gamma_{31})} + \frac{z_{12}z_{23}z_{31}}{(\omega_{31} + 2\omega + i\gamma_{31})(\omega_{21} + \omega + i\gamma_{21})} + \frac{z_{12}z_{23}z_{31}}{(\omega_{31} - 2\omega - i\gamma_{31})(\omega_{21} - \omega - i\gamma_{21})} + \frac{z_{12}z_{23}z_{31}}{(\omega_{23} - 2\omega - i\gamma_{23})(\omega_{31} + \omega + i\gamma_{31})} + \frac{z_{12}z_{23}z_{31}}{(\omega_{32} + 2\omega + i\gamma_{32})(\omega_{21} - \omega - i\gamma_{21})} + \frac{z_{12}z_{23}z_{31}}{(\omega_{21} + 2\omega + i\gamma_{21})(\omega_{31} + \omega + i\gamma_{31})} + \frac{z_{31}^2(z_{11} - z_{33})}{(\omega_{31} - \omega - i\gamma_{31})(\omega_{31} - 2\omega - i\gamma_{31})} \right\}$$

where ω is the pump frequency, e is the electron charge, N_e is the average bulk doping density of the MQW structure, z_{ij} , $\hbar\omega_{ij}$, and $\hbar\gamma_{ij}$ are the matrix element of electron z-position, transition energy, and transition linewidth, respectively, between states i and j . For calculations, we have assumed all electron population to reside in state 1 and used the computed values of z_{21} , z_{31} , and z_{32} as shown in Figure 1a and $(z_{11} - z_{33}) = -1.86 \text{ nm}$. We also used experimentally measured values of $\hbar\omega_{21} \approx 150 \text{ meV}$, $\hbar\omega_{31} \approx 248 \text{ meV}$, $2\hbar\gamma_{12} \approx 24.8 \text{ meV}$, $2\hbar\gamma_{13} \approx 29.2 \text{ meV}$, and $N_e = 1.13 \times 10^{18} \text{ cm}^{-3}$ as discussed in the Supporting Information. Finally, we have assumed $\hbar\gamma_{23} = 15 \text{ meV}$ as this transition linewidth cannot be deduced from simple absorption measurements.

Supporting Information

Supporting Information is available from Wiley Online Library or from the author

Acknowledgements

This work was supported, in part, by the AFOSR Grant No. FA9550-14-1-0105 (to A.A. and M.A.B.) and the ONR MURI Grant No. N00014-10-1-0942 (to A.A.). Walter Schottky Institute group acknowledges support from the excellence cluster "Nano Initiative Munich (NIM)". Sample fabrication was carried out in the Microelectronics Research Center at the University of Texas at Austin, which is a member of the National Nanotechnology Infrastructure Network. The authors would also like to acknowledge help of Dr. Yanan Wang in Prof. Jiming Bao group at the University of Houston with facilitating e-beam processing of the earlier generation of samples.

Received: December 3, 2015

Revised: December 24, 2015

Published online:

- [1] J. B. Pendry, *Science* **2008**, 322, 71.
 [2] N. Segal, S. Keren-Zur, N. Hendler, T. Ellenbogen, *Nat. Photonics* **2015**, 9, 180.
 [3] C. Argyropoulos, P. Y. Chen, F. Monticone, G. D'Aguzzo, A. Alu, *Phys. Rev. Lett.* **2012**, 108, 263905.

- [4] J. Lee, M. Tymchenko, C. Argyropoulos, P. Y. Chen, F. Lu, F. Demmerle, G. Boehm, M. C. Amann, A. Alu, M. A. Belkin, *Nature* **2014**, 511, 65.
 [5] M. Tymchenko, J. S. Gomez-Diaz, J. Lee, N. Nookala, M. A. Belkin, A. Alu, *Phys. Rev. Lett.* **2015**, 115, 207403.
 [6] G. X. Li, S. M. Chen, N. Pholchai, B. Reineke, P. W. H. Wong, E. Y. B. Pun, K. W. Cheah, T. Zentgraf, S. Zhang, *Nat. Mater.* **2015**, 14, 607.
 [7] O. Wolf, S. Campione, A. Benz, A. P. Ravikumar, S. Liu, T. S. Luk, E. A. Kadlec, E. A. Shaner, J. F. Klem, M. B. Sinclair, I. Brener, *Nat. Commun.* **2015**, 6, 7667.
 [8] S. Keren-Zur, O. Avayu, L. Michaeli, T. Ellenbogen, *ACS Photonics* **2016**, 3, 117.
 [9] E. Almeida, G. Shalem, Y. Prior, *Nat. Commun.* **2016**, 7, 10367.
 [10] N. Nookala, J. Lee, M. Tymchenko, J. S. Gomez-Diaz, F. Demmerle, G. Boehm, K. Lai, G. Shvets, M.-C. Amann, A. Alu, M. A. Belkin, unpublished.
 [11] R. W. Boyd, *Nonlinear Optics*, Academic Press, New York, NY, USA **2008**.
 [12] Y. R. Shen, *The Principles of Nonlinear Optics*, WileyInterscience, Hoboken, NJ, USA **2002**.
 [13] F. B. P. Niesler, N. Feth, S. Linden, J. Niegemann, J. Gieseler, K. Busch, M. Wegener, *Opt. Lett.* **2009**, 34, 1997.
 [14] W. J. Fan, S. A. Zhang, K. J. Malloy, S. R. J. Brueck, N. C. Panou, R. M. Osgood, *Opt. Express* **2006**, 14, 9570.
 [15] E. Rosencher, A. Fiore, B. Vinter, V. Berger, P. Bois, J. Nagle, *Science* **1996**, 271, 168.
 [16] F. Capasso, C. Sirtori, A. Y. Cho, *IEEE J. Quantum Electron.* **1994**, 30, 1313.
 [17] E. Rosencher, P. Bois, J. Nagle, S. Delaitre, *Electron. Lett.* **1989**, 25, 1063.
 [18] M. M. Fejer, S. J. B. Yoo, R. L. Byer, A. Harwit, J. S. Harris, *Phys. Rev. Lett.* **1989**, 62, 1041.
 [19] K. Vijayraghavan, Y. Jiang, M. Jang, A. Jiang, K. Choutagunta, A. Vizbaras, F. Demmerle, G. Boehm, M. C. Amann, M. A. Belkin, *Nat. Commun.* **2013**, 4, 2021.
 [20] M. Jang, R. W. Adams, J. X. Chen, W. O. Charles, C. Gmachl, L. W. Cheng, F. S. Choa, M. A. Belkin, *Appl. Phys. Lett.* **2010**, 97, 141103.
 [21] M. A. Belkin, F. Capasso, A. Belyanin, D. L. Sivco, A. Y. Cho, D. C. Oakley, C. J. Vineis, G. W. Turner, *Nat. Photonics* **2007**, 1, 288.
 [22] I. Vurgaftman, J. R. Meyer, L. R. RamMoham, *IEEE J. Quantum Electron.* **1996**, 32, 1334.
 [23] J. R. Meyer, C. A. Hoffman, F. J. Bartoli, E. R. Youngdale, L. R. RamMoham, *IEEE J. Quantum Electron.* **1995**, 31, 706.
 [24] J. S. Gomez-Diaz, M. Tymchenko, J. Lee, M. A. Belkin, A. Alu, *Phys. Rev. B* **2015**, 92, 125429.
 [25] K. L. Vodopyanov, V. Chazapis, C. C. Phillips, B. Sung, J. S. Harris, *Semicond. Sci. Technol.* **1997**, 12, 708.
 [26] K. L. Vodopyanov, K. O'Neill, G. B. Serapiglia, C. C. Phillips, M. Hopkinson, I. Vurgaftman, J. R. Meyer, *Appl. Phys. Lett.* **1998**, 72, 2654.
 [27] H. Asai, Y. Kawamura, *J. Appl. Phys.* **1990**, 68, 5890.
 [28] P. Vonallmen, M. Berz, G. Petrocelli, F. K. Reinhart, G. Harbeke, *Semicond. Sci. Technol.* **1988**, 3, 1211.
 [29] We note that a 700-nm-thick nonlinear metasurface with SHG slope efficiency (cf. Figure 3c) of 0.45 mW W^{-2} for low-intensity pumping at $\lambda \approx 10 \mu\text{m}$ was reported recently in ref. [7]. Using the pump focal spot diameter of $100 \mu\text{m}$ in ref. [7], we deduce the largest nonlinear element of this metasurface to be $\approx 0.3 \times 10^6 \text{ pm V}^{-1}$ or more than 3 times smaller than that of the metasurface presented in this work. The metasurface in ref. [7] was designed using unetched split-ring resonators and operated in transmission mode. According to our calculations shown in Figure 2c–e, this metasurface design is expected to provide lower conversion efficiency compared to the metasurface

design presented in this work, assuming identical MQW nonlinearity. We can explain the results reported in ref. [7] by assuming that the value of intersubband nonlinearity of the MQW heterostructure in ref. [7] is more than one order of magnitude larger than that of the MQW heterostructure used in this work (the value of MQW intersubband nonlinearity is not given in ref. [7]). We then expect that the nanoresonators presented in this work combined with MQW materials used in ref. [7] may be able to produce metasurfaces with $\chi_{yx}^{(2)} > 10^7$ pm V⁻¹ and SHG conversion efficiencies well over 1%.

- [30] C. Y. Wang, L. Kuznetsova, V. M. Gkortsas, L. Diehl, F. X. Kartner, M. A. Belkin, A. Belyanin, X. Li, D. Ham, H. Schneider, P. Grant, C. Y. Song, S. Haffouz, Z. R. Wasilewski, H. C. Liu, F. Capasso, *Opt. Express* **2009**, *17*, 12929.
- [31] S. Kalchmair, R. Gansch, S. I. Ahn, A. M. Andrews, H. Detz, T. Zederbauer, E. Mujagic, P. Reininger, G. Lasser, W. Schrenk, G. Strasser, *Opt. Express* **2012**, *20*, 5622.
- [32] C. Walther, G. Scalari, M. I. Amanti, M. Beck, J. Faist, *Science* **2010**, *327*, 1495.